Polyoxometalates

RESEARCH ARTICLE

Proton conduction facilitates the hydrogen evolution reaction in heptamolybdate-protected SnO_2 nanocore

Laxmikanta Mallick §, Hirak Kumar Basak§, and Biswarup Chakraborty

Department of Chemistry, Indian Institute of Technology Delhi, Hauz Khas, New Delhi 110016, India
§ Laxmikanta Mallick and Hirak Kumar Basak contributed equally to this work.

Received: 14 July 2026; **Revised:** 15 October 2026; **Accepted:** 3 November 2026

Address correspondence to cbiswarup@chemistry.iitd.ac.in

Cite This: *Polyoxometalates*, 2027, *6*, 9140175 https://doi.org/10.26599/POM.2026.9140175

ABSTRACT: Recently, the Anderson-type heptamolybdate $[Mo_7O_{24}]^{6-}$ ion has been used as an inorganic ligand to protect various metal oxy-hydroxides (FeOOH and $Ni_xFe_{1-x}OOH$) and oxides (SnO_2 and CeO_2), and these unique varieties of materials are employed as electrode materials for water oxidation and nitrate reduction. Herein, $[Mo_7O_{24}]^{6-}$ covalently connected to a SnO_2 nanocore, namely $Mo_x@SnO_2$, is prepared through a hydrothermal route and has been fabricated on a 1 cm^2 surface of a conducting carbon support to study proton conduction and electrocatalytic proton reduction. The $Mo_x@SnO_2$ fabricated carbon cloth (CC) exhibits the maximum proton conductivity of 15.34 × 10^{-3} S cm^{-1} at pH 3.65 and room temperature, which increased linearly with the increment in cell temperature and reached 32.47 × 10^{-3} S cm^{-1} at 318 K. Under similar conditions, the bare SnO_2 fabricated on CC shows relatively low proton conductivity, highlighting the importance of POM ligands on $Mo_x@SnO_2$ to facilitate proton conduction with an extremely low activation energy of 0.13 eV, indicative of proton shuttling through the Grotthuss pathway. Further, the facile proton conduction on $Mo_x@SnO_2$ and the redox participation of POMs, as depicted from cyclic voltammetric studies, enable electrocatalytic hydrogen evolution reaction (HER) under mild acidic conditions, delivering an onset potential of -0.4 V vs RHE and a nearly two-fold higher catalytic current at -0.9 V compared to that observed for SnO_2. The electrokinetic study has confirmed that the improved performance of $Mo_x@SnO_2$ over SnO_2 is due to enhanced charge-transfer kinetics. This study showcases a new role for covalently attached heptamolybdate anions on SnO_2, facilitating proton relay and reduction.

KEYWORDS: heptamolybdate, SnO_2 core, proton conductivity, electrocatalyst, hydrogen evolution reaction

Just Accepted

1 Introduction.

Rapid population growth results in exponential growth in global energy consumption, as reported by the US DOE, with about 34% by 2050.[1] Subsequently, energy consumption challenges the depletion of fossil fuels, which are the primary source of traditional energy.[2] To minimise the consumption of traditional energy, some cleaner energy devices have recently been developed that convert chemical energy to electric energy; among them, fuel cells, proton exchange membrane fuel cells (PEMFCs), and polymer electrolyte membrane fuel cells (PEMFCs) have attracted significant attention.[3] Among the different devices, the proton exchange membrane fuel cell (PEMFC) is inferred as a promising technology for curbing the environmental and energy problem, due to its unique benefits such as high energy conversion efficiency (>60%), operating temperature (80 °C), zero greenhouse gas emission, rapid startup and convenient integration, where the proton exchange membrane (PEM) is the heart of the system, which enables proton conduction and provides isolation within the fuel cell.[1,2] Nafion is a widely used proton-conducting material due to its high conductivity (> 10^{-2} Scm^{-1}) and excellent chemical stability. It was first used as a proton-conducting material and widely commercialised. However, the performance degradation at temperatures above 100 °C is due to dehydration, disruption of proton transport channels, reduced conductivity, and fluorine leaching and contamination in water, which limit its potential application.[3]

Due to high crystallinity and porosity, tunable topography, variable chemical functionality, surface functionalization possibilities, and controllable guest adaptability inside the pores, different crystalline porous materials such as metal–organic frameworks (MOFs), hydrogen-bonded organic frameworks (HOFs), covalent organic frameworks (COFs), and porous polymers (POPs) grab attention as potential candidates for proton-conducting materials. materials. [4–7] The proton conductivity in framework-based materials mostly depends on the number of proton sources and the H-bonding pathway.[1] Polyoxometalates (POMs) are aqueously soluble and cost-effective, which makes them a greener and environmentally friendly material. Crystalline molecular materials including polyoxometalates (POMs)[8–11] have gained significant interest for proton conduction due to their modular assembly, high stability, and chemical tunability.[12] Notably, the high density of oxygen atoms on the surface of POMs provides multiple sites for proton shuttling, and the nanoscale anionic clusters on their surface exhibit a lower charge density due to negative charge delocalisation, which facilitates the dynamic proton adsorption and migration.[2] However, POM-based frameworks or materials[13]

are relatively less explored. Nakamura et al. first conducted a detailed study of the proton conductivity of POMs using dodecamolybdophosphoric acid ($H_3PMo_{12}O_{40}{\cdot}29H_2O$) and dodecatungstophosphoric acid[14] Thereafter, various POM-based proton conductors have been developed and mostly studied in solid-state media. Das's group reported recently various polyoxomolybdates[3,10,15,16] and polytungstate clusters, such as xerogel $\{W_{72}Fe_{30}\}_{XG}$, and polymer-based polyoxometalate processed membranes of 5% $\{W_{72}Fe_{30}\}$+PA@m-PBI, which show facile proton conduction (1.71×10^{-2} S cm^{-1} S cm^{-1})[3] and 1.59×10^{-1} S cm^{-1} S cm^{-1},[17] under relative humidity of 98%. Recently, Chakraborty and co-workers reported a triazole-containing polymer and studies of proton conductivity of 2.5×10^{-2} S cm^{-1} in the liquid phase, which opens the door to investigating proton conduction under real operating conditions.[18] In a subsequent study, the polymer showing outstanding proton shuttling has been fabricated as a PEM membrane, and the same polymer showed notably low overpotential (311 mV at 10 mA cm^{-2}) for the hydrogen evolution reaction (HER) when used as a cathode.[19] Solution-state proton conductivity is a more realistic assessment than solid-state measurements, as real-world membrane use in proton conduction involves two solutions separated by a membrane.[18,19] Proton conductivity is often facilitated by proton adsorption, which is an essential step for the electrocatalytic hydrogen evolution reaction (HER). [18–21]

Herein, heptamolybdate-stabilized SnO_2 has been prepared and fabricated on a carbon support to study intrinsic proton relay in the solution state. Variable pH and temperature impedance studies were performed to obtain the proton conductivity and activation barrier to understand the shuttling pathway. Further, the $Mo_x@SnO_2$ fabricated electrode was used for the study of electrocatalytic HER under mild acidic pH conditions to show the dual function of the material. Saira et al. demonstrated that hollow-architecture SnO_2 is an active catalyst for HER, but low Ru loading exhibits markedly enhanced HER activity and long-term stability by overcoming the sluggish kinetics associated with pristine SnO_2.[22] Early studies demonstrated that polyoxometalates (POMs) can serve as robust molecular platforms for stabilizing normally inert transition metal-aqua complexes and promoting efficient proton-coupled electron transfer (PCET) in the hydrogen evolution process (HER). In particular, POM-supported Cu(II)-aqua complexes were effective for HER under near-neutral conditions[23] and a nickel-containing polyoxovanadate was used to electrochemically transform inactive $[Ni(H_2O)_6]^{2+}$ into an efficient and stable homogeneous HER catalyst with low overpotential,[24] demonstrating the unique role of POMs in modulating the electronic structure and catalytic activity of transition metal centers. POM clusters preferably contribute to HER through electron buffering and via tuning of the electronic structure of the complex. During the electrocatalytic events, POMs undergo reversible multi-electron redox shuttling[25] and also act as the active site for hydrogen adsorption due to the presence of oxo terminals and moderate adsorption free energy of hydrogen intermediates (ΔG_{H^*}). Further coordination of the metal center through oxo-terminals of the POMs modulates the electronic state, redistributing the electron density to nearby metal centers or metal–oxide interfaces.[26] POMs are also capable of free diffusion of protons or rapid shuttling. The oxygen-rich framework (M=O, bridging M-O-M, and surface M-OH groups) accumulates protons at the catalyst surface, accelerating water splitting; in hydroxylated systems, fewer W^V-OH sites can even reduce water to H_2.[26,27] Finally, POM containing catalysts prefer the proton-coupled-electron-transfer (PCET) pathway ($M\text{-}O + e^- + H^+ \rightleftharpoons M\text{-}OH$), which reduce the energy barrier to stabilize the HER intermediates which allow transition metal containing POM complexes as active HER catalysts in near-neutral conditions.[26,27] Despite wide use of SnO_2 in FTO- or ITO-based electrode fabrication, the electrocatalytic performance is not impressive. Further, the limited HER studies with pristine SnO_2 are available in literature. Herein, a comparative HER performance of $Mo_x@SnO_2$ material with bare SnO_2 is performed to understand the role of POM ligands present in the surface of SnO_2 nanocore.

2 Experimental Section

2.1 Synthesis of SnO_2, and $Mo_x@SnO_2$ nanocore

Tin (II) chloride (14 mg, 0.06 mmol) was dissolved in 8 mL of deionised water in a 20 mL glass vial. A freshly prepared 0.2 M NaOH solution was added dropwise until the pH reached 6.8–7.0. The reaction mixture was brought to a final volume of 10 mL with deionised water, with a pH of approximately 4.5. The mixture was transferred to a 25 mL Teflon-lined stainless-steel autoclave and heated at 75 °C for 24 h. After cooling to room temperature, the reaction mixture was transferred to centrifuge tubes. The yellow precipitate was collected by centrifugation and washed with deionized water. This process was repeated twice to remove residual impurities. Finally, the yellow precipitate was dried at 60 °C for 4 h in an air oven and ground with an agate mortar for subsequent characterization and experiments.

Just Accepted

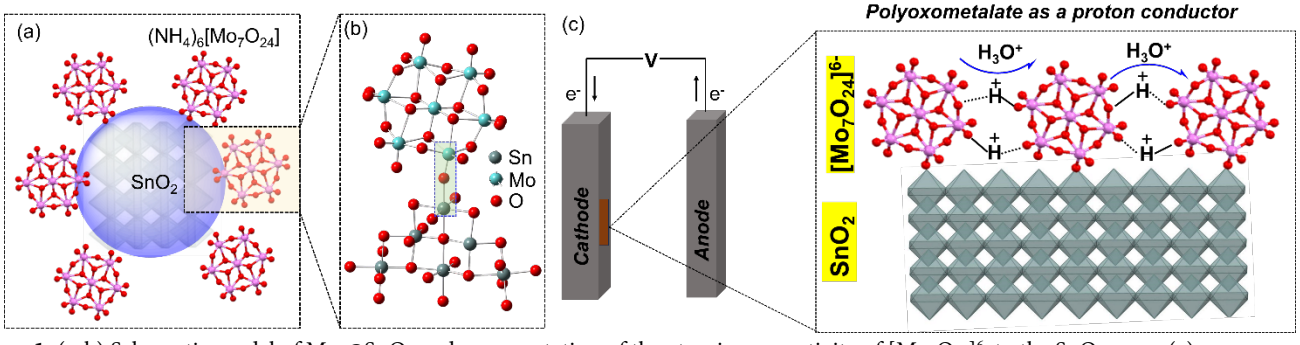


Figure 1. (a-b) Schematic model of $Mo_x@SnO_2$ and representation of the atomic connectivity of $[Mo_7O_{24}]^{6-}$ to the SnO_2 core. (c) Electrocatalytic cell diagram with $Mo_x@SnO_2$ fabricated cathode and its proton conduction through hydrogen bonding at the oxo-terminals of POM anions.

Aqueous dispersed $Mo_x@SnO_2$ nanoparticles were prepared hydrothermally and purified through a repeated cycle of NaCl wash followed by dialysis against deionized water, as reported in the literature.[28]

2.2 Proton conductivity

To study the proton conductivity, SnO_2 and $Mo_x@SnO_2$ nanoparticles were dispersed in 1-2 % Nafion in ethanol solution, and the resultant mixture was drop-cast on a 1 cm^2 geometric surface area of the carbon cloth (CC: 2 x 1 cm). The mass loading of the material was 10±1 mg cm^{-2}. The proton conductivity was measured in a standard three-electrode set-up, taking $Mo_x@SnO_2$/CC as the working electrode, Ag/AgCl as the reference electrode, Pt wire as the counter electrode, and using an aqueous electrolyte of different proton concentrations. Electrochemical AC impedance spectroscopy (EIS) studies were carried out over a frequency range of 0.01 to 1 MHz with an applied AC voltage of 10 mV and a DC voltage of -1.8 V vs Ag/AgCl. Impedance spectra were collected over a range of pH values (3-5) and temperatures (303 K-318 K). The conductivity was determined from the Nyquist plot using the equation: $\sigma = L / (A \cdot R)$, where σ is the proton conductivity (S cm^{-1}), L is the thickness (cm), and A is the cross-sectional area (cm^2) of the electrode. From the variable-temperature EIS studies, the activation energy was calculated from the Arrhenius equation (Eq. 1):

$$\sigma = \sigma^o \exp\left(-\frac{E_a}{k_B T}\right) \qquad \text{Equation 1}$$

Where σ is the proton conductivity, k_B is the Boltzmann constant, σ^0 is the pre-exponential factor, and T is the temperature.

2.3 Hydrogen evolution reaction (HER)

The electrocatalytic hydrogen evolution reaction (HER) activities of bare SnO_2 and $Mo_x@SnO_2$ were systematically studied using a standard three-electrode electrochemical cell in 0.1 M acetate buffer solution (pH=5±0.2) as the electrolyte. SnO_2 and $Mo_x@SnO_2$ were deposited on CC as the working electrode, with an Ag/AgCl reference electrode and a graphite (diameter: 3 mm) rod counter electrode. HER performance was evaluated by linear sweep voltammetric study (LSV) at 1 mV · dec-1, while the LSV polarograms were 50% iR compensated. The Tafel slope was obtained from the linear sweep voltammetry (LSV) polarisation curves by plotting the overpotential (η) against the logarithm of the current density (log j) according to Equation (2).

$$\eta_{OER} = b log \frac{j}{j_0} \qquad \text{(Equation 2)}$$

where η denotes overpotential (V); j, current density (mA cm^{-2}); j_0, exchange current density (mA cm^{-2}); and b, Tafel slope (mV dec^{-1}).[29] The electrochemically active surface area (ECSA) was determined from the double-layer capacitance (C_{dl}), which was derived from cyclic voltammograms measured in the non-faradaic region at scan rates of 10-200 mV s^{-1}. The ECSA was computed according to Equation (3), assuming the specific capacitance Cs of 0.04 mF cm-2 in similar electrolyte conditions.[30]

$$\eta_{OER} = b log \frac{j}{j_0} \qquad \text{(Equation 3)}$$

Electrochemical impedance spectroscopy (EIS) measurements were performed at an applied potential of −0.8 V vs. RHE over a frequency range of 100 kHz to 1 mHz. The Nyquist plots were fitted using an equivalent RC circuit, and the charge-transfer resistance (R_{ct}) was determined from the circuit fitting of the high-frequency semicircle.[31]

3 Results and Discussion.

3.1 Heptamolybdate-coordinated SnO_2

Recently, Chakraborty and co-workers reported that the Anderson-type $[(NH_4)_6Mo_7O_{24}]$ ion can be used to stabilise the FeO(OH)[32], $Ni_xFe_{1-x}FeO(OH)$,[33] and also SnO_2 QD with a 3-4 nm overall particle size (Figure 1a). The first two materials were used to fabricate an anode with remarkable electrocatalytic oxygen evolution reaction (OER), although a significant amount of molybdate leaching in alkaline medium results in instability of the POM-protected metal oxy-hydroxide core structure. The $Mo_x@SnO_2$ material is distinct as it has a p-block metal oxide in the core, with a significant amount of oxygen vacancies. Further, SnO_2 nanoparticles are reported to be more conductive than transition metal oxides. Therefore, vacancy-rich $Mo_x@SnO_2$ material was used to fabricate a cathode to study electrocatalytic nitrate reduction to selectively produce ammonia.[28] The strong covalent linkage of the molybdate (Mo^{VI}-O-Sn^{IV}) to the SnO_2 core preserves the material for a longer period of time in water as well as under reductive conditions and acidic pH (Figure 1b). Owing

Just Accepted

to the high aqueous stability of the $Mo_x@SnO_2$, the oxo terminals of the isopolymolybdate ligands serve as proton adsorption sites, and its notable cathodic performance leads to the use of this unique material for proton conductivity studies and subsequent hydrogen evolution reaction at acidic pH (Figure 1c). The $Mo_x@SnO_2$ material was synthesised using the reported procedure, and powder X-ray diffraction (PXRD) shows reflections of the cubic SnO_2 phase between 2θ values of 10-80° (JCPDS file No. 01-01-70-4177) (Figure 2a), similar to that reported earlier.[28,34] Subsequently, high-resolution transmission electron microscopy (HRTEM) revealed well-defined (110) and (002) crystal facets with an interplanar spacing of 0.325 nm and 0.164 nm (Figure 2b, Figure S1-S2). SAED further confirmed the crystalline SnO_2 core (Figure 2b, inset). Field-emission scanning electron microscopy (FESEM) images and simultaneous energy-dispersive X-ray spectroscopy (EDX) elemental mapping indicate a homogeneous distribution of Sn, Mo, and O (Figure 2c-2f).

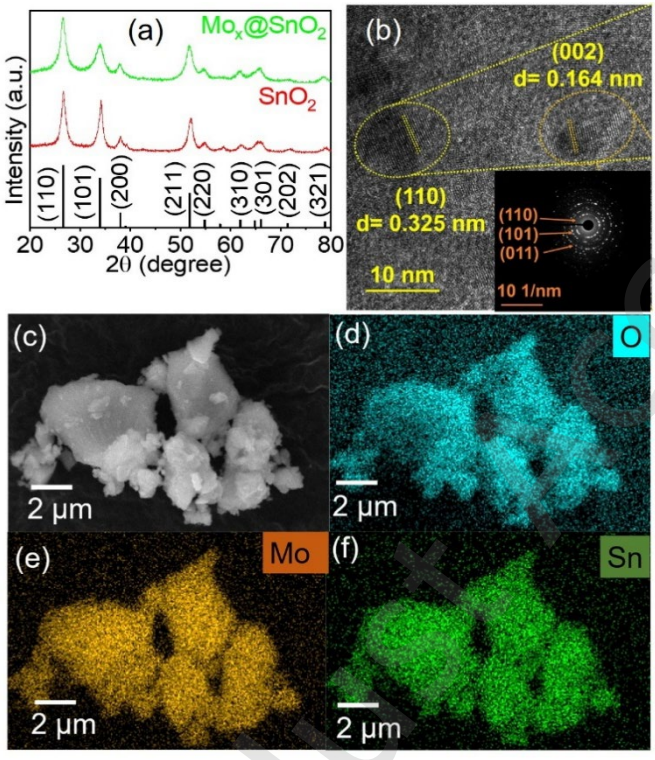


Figure 2. (a) PXRD pattern of as-synthesized SnO_2, $Mo_x@SnO_2$, and bar diagram of the simulated pattern from reported JCPDS data. (b) HRTEM image of a single nanoparticle of $Mo_x@SnO_2$ showing (110) (101) and (011) lattice fringes (Inset: SAED pattern). (c) FESEM images of $Mo_x@SnO_2$. (d-f) FESEM-EDX elemental (Sn, Mo, and O) mapping of a selected region of the $Mo_x@SnO_2$ material.

3.2 Proton conductivity study.

The proton conductivities of $Mo_x@SnO_2$ were measured by the AC EIS studies at a constant applied potential (experimental section), and the data are presented through Nyquist plots. The semicircular arcs of the individual plots were fitted into an equivalent R||C circuit. The diameter of the arc is highly dependent on the pH of the electrolyte. As seen from Figure 3a, the solution resistance (R_s) for the electrolyte at different pH levels (pH: 4.57, 4.23, 3.86, 3.65) at 30°C (303 K) was almost constant, 10.75 Ω while the R_{ct} values gradually dropped with the decrease in pH of the electrolyte. The proton conductivity was measured at different pH values (pH: 4.57, 4.23, 3.86, 3.65) at 30°C (303 K) from the Nyquist plot and using the relation (Figure 3, Figure S3, Table S1-S2). At pH 4.57, the conductivity value was calculated to be 9.69×10^{-3} S cm^{-1} (Figure 3a). Addition of dil. acid resulted in decreasing the pH of the electrolyte, and consequently the proton conductivity gradually increased to 15.34×10^{-3} S cm^{-1} at pH 3.65 (Figure 3b). The conductivity of $Mo_x@SnO_2$ is higher than that of bare SnO_2 at pH 3.65 (Figure S3). At pH 3.65, the proton conductivity of $Mo_x@SnO_2$ increased almost linearly when the cell temperature was raised from 303 K to 318 K, and it reached 32.47×10^{-3} S cm^{-1} (Figure 3c). The proton conductivity of bare SnO_2 and carbon cloth (CC) support itself at pH 3.65 is 1.58×10^{-3} S cm^{-1} and 1.09×10^{-3} S cm^{-1}, respectively, at 318 K, which highlights a better conductivity of $Mo_x@SnO_2$ than the bare SnO_2 (1.92×10^{-3} S cm-1) (Figure 3d-3h, Figure S3, Table S1-S2). At a given temperature, the higher proton conductivity of $Mo_x@SnO_2$ compared to bare SnO_2 and its enhancement with increasing temperature and increasing proton concentration demonstrate the vital role of the heptamolybdate clusters present on the surface of SnO_2 in the proton conduction of $Mo_x@SnO_2$.

Proton hopping generally proceeds through two distinct pathways, and it can be assessed by evaluating the activation energy. The activation energy (E_a) for the proton conductivity can be experimentally determined by recording EIS at variable temperatures (Figure 3i) and correlating the change in proton conductivity with temperature. Upon increasing the cell temperature, the diameter of the arc-shaped Nyquist plot became smaller, which corroborated the drop in charge transfer resistance across the double layer. Consequently, it gave a linear increment of conductance with temperature. Fitting the variable-temperature conductivity data into the Arrhenius relation and using the slope of the linear fit of the log(σ) versus 1/T plot gave the activation barrier energy of proton hopping. The experimentally determined E_a for $Mo_x@SnO_2$ was obtained as 0.13 eV, which is lower than bare SnO_2 (E_a=0.19 eV) and carbon cloth (E_a=0.21 eV) (Figure 3i). The activation energy (E_a) suggests that the proton-transfer pathway in $Mo_x@SnO_2$ follows the Grotthuss mechanism,[35] which is dependent on the hydrogen-bond network of water molecules, enabling proton conduction, and is accompanied by hydrogen-bond breakdown and recombination. Delocalisation of negative charges on heptamolybdates' surfaces and the "oxo" terminals facilitate the adsorption and desorption of protons on the POM surface (Figure 1c).[36] POMs also have entirely hydrophilic cluster structures that are rich in oxygen, and hydrogen bonds can form readily in the vicinity of these abundant oxygen sites.[37] Proton transport benefits from the high reversibility of this dynamic hydrogen-bonding formation and dissociation mechanism (Figure 1c).[35,38,39] However, establishing a specific proton conduction mechanism in POM materials is quite difficult due to various factors such as the activation barrier, proton concentration, acidity of the hydrogen-bonding pathway (whether continuous or closed loops), the proton sources, and proton diffusion dynamics.[1] Previously,

Just Accepted

several literature reports on solid-state proton conductivity with superconducting properties, with activation energies of 0.17eV to 0.60 eV, in the high-temperature range 50°C-100°C (Table S3). Here, a solution-based proton conductivity was performed with a Anderson-type polyoxometalate protected with a well-known electrode, SnO_2, with low activation energy (0.13 eV) and high proton conductivity 32.47 × 10^{-3} S cm^{-1} at 45°C (318K) compared to Anderson type polyoxometalates-based metal–organic frameworks (POMOFs) used such as $[Co_3(Bip)_2(H_2O)_{10}(TeMo_6O_{24})]$ (CUST-861) of 2.96 × 10^{-2} S cm^{-1} at 45°C reported by Cui et. al [40]

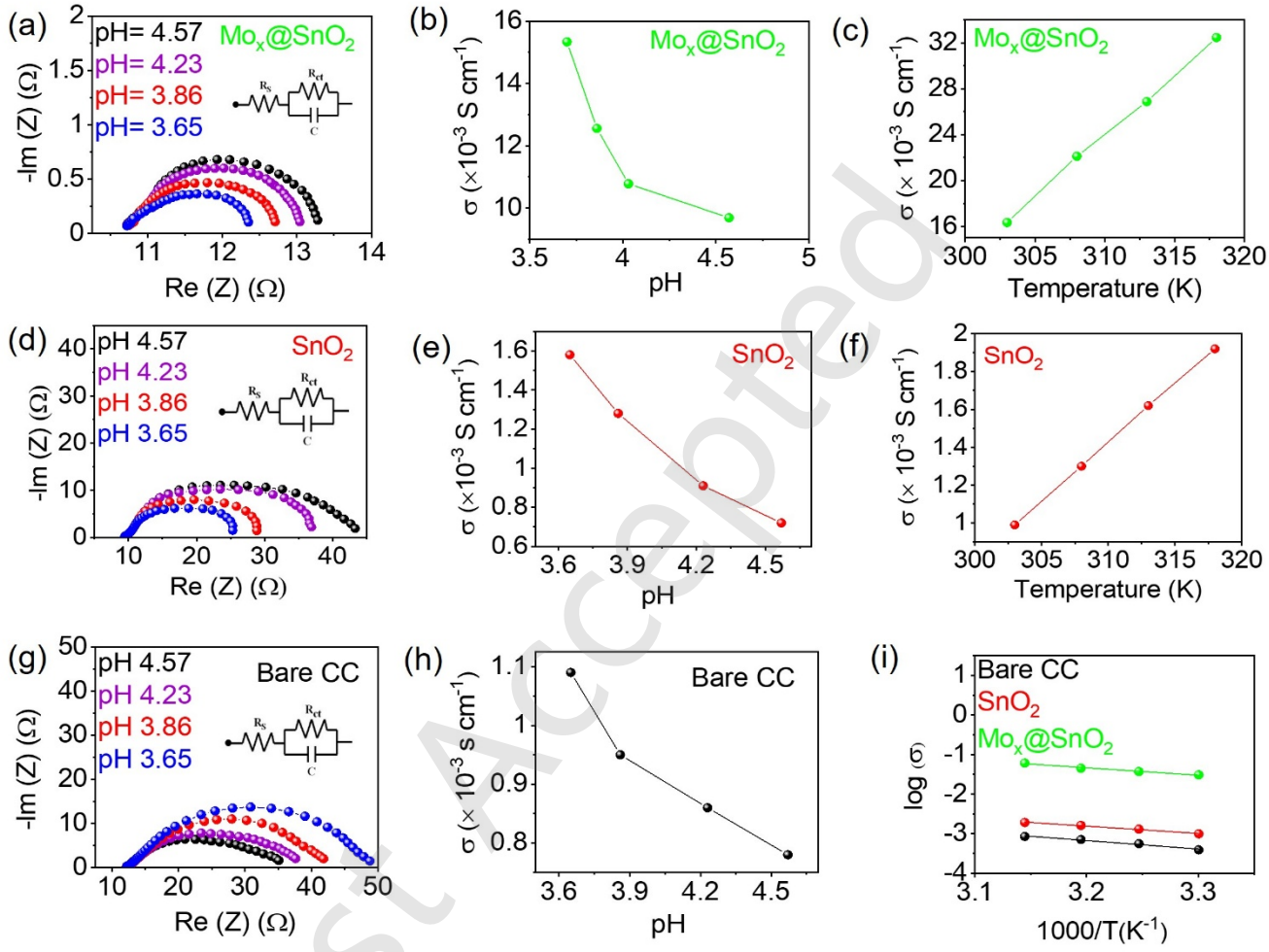


Figure 3. (a) Nyquist plots (from EIS) at different pH for $Mo_x@SnO_2$, (b) Plot of proton conductivity at different pH for $Mo_x@SnO_2$, (c) Plot of proton conductivity at different temperatures for $Mo_x@SnO_2$, (d) Nyquist plots (from EIS) at different pH for SnO_2, (e) Plot of proton conductivity at different pH for SnO_2, (f) Plot of proton conductivity at different temperatures for SnO_2. (g) Nyquist plots (from EIS) at different pH for carbon cloth (CC), (h) Plot of proton conductivity at different pH for carbon cloth (CC), and (i) Arrhenius plot for the activation energy of carbon cloth (black curve), SnO_2 (purple curve), and $Mo_x@SnO_2$ (blue curve).

Just Accepted

3.3 Electrocatalytic hydrogen evolution reaction (HER) study.

Cyclic and linear sweep voltammetry (CV and LSV) were carried out on SnO_2 and $Mo_x@SnO_2$ using a three-electrode configuration in an acetate buffer (pH 3.65). For the HER study, owing to its higher proton conductivity, the acetate buffer of a lower pH value was selected. The CV study was performed within the potential window of 0.4 to -1.0 V (Figure 4, S4a-S4b). $Mo_x@SnO_2$ material showed redox features associated with the redox features of POM, as reported earlier. A slight improvement in the catalytic current with the progress of CV cycles, followed by stabilisation after 5-10 CV cycles, was noticed (Figure 4b). CV polarisation curves of $Mo_x@SnO_2$ exhibit a broad cathodic feature around −0.15 V, which can be assigned to the overlapping reduction processes of surface Sn (IV) species and Mo (VI) centres. The broadening of the redox response indicates the coexistence of multiple electroactive sites and strong electronic (covalent) interactions between the $[Mo_7O_{24}]^{6-}$ and the SnO_2 core (Figure 4a-4b). By contrast, bare SnO_2 exhibits relatively sharper redox features for the reduction of surface Sn species (Figure 4a-4c). In the LSV polarisation curves of both materials, the onset of the HER partly overlaps with these redox processes, resulting in less pronounced individual peaks. The HER onset potentials of SnO_2 and $Mo_x@SnO_2$ are similar (ca. -0.4 V vs RHE), but upon further application of cathodic potential during LSV, $Mo_x@SnO_2$ shows a significant enhancement of the cathodic current density. To

correctly compare the HER kinetics, Tafel plots were generated from the LSV polarisation curves. A Tafel slope of 143 mV dec^{-1} for $Mo_x@SnO_2$ was obtained, which is significantly lower than that of SnO_2 and CC (Figure 4d). It is worth mentioning that, at an applied potential of ca. −0.9 V, the current density of $Mo_x@SnO_2$ is nearly two times higher than that of pristine SnO_2, demonstrating the positive role of encapsulating heptamolybdate. The improved performance can be attributed to the synergistic interaction between POM and SnO_2, which enables charge transfer, increases the density of electrochemically active sites, and promotes more efficient proton reduction kinetics. Furthermore, cyclic voltammetry measurements in the non-faradaic region showed a higher capacitive current response for $Mo_x@SnO_2$ (0.14 mF cm^{-2}), indicating a larger electrochemically active surface area (ECSA) of $Mo_x@SnO_2$ (2.8 cm^2) compared to SnO_2 (C_{dl}: 0.09 mF cm^{-2}, ECSA: 1.8 cm^2) (Figure 4e, Figure S5). Electrochemical impedance spectroscopy (EIS) analyses showed that $Mo_x@SnO_2$ exhibited a much lower charge-transfer resistance (R_{ct} of ~20 Ω), indicating improved interfacial electron transfer and enhanced conductivity at the electrode–electrolyte interface at an applied potential of -0.7 V (vs RHE) (Figure 4f). Moreover, the electrochemical double-layer capacitance (C_{dl}) values showed a much higher C_{dl} for $Mo_x@SnO_2$ than for bare SnO_2, which confirmed the increased number of exposed electrochemically active sites. The $Mo_x@SnO_2$ catalyst delivers a 17±3 mA cm^{-2} current density for 60 h at −0.8 V versus RHE for 60 hours during the electrochemical chronoamperometric HER study (Figure 5a), and post-CA-HER LSV delivered an almost comparable catalytic current (Figure 5b). At the beginning of CA, a slight drop in the current density was noticed, while throughout the time *j* was maintained at >15 mA cm^{-2} .

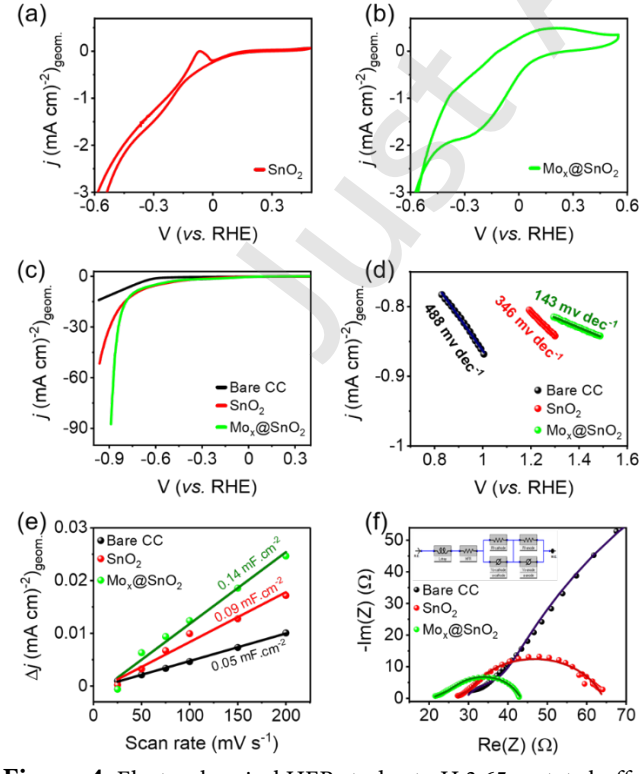


Figure 4. Electrochemical HER study at pH 3.65 acetate buffer: cyclic voltammograms recorded for (a) SnO_2 and (b) $MO_x@SnO_2$ within 0.4 V to -0.6 V. (c) Linear sweep voltammetric polarisation curves, (d) Tafel plots, (e) double layer capacitance, and (f) Nyquist plot obtained from the EIS study with carbon cloth (CC), SnO_2, and $Mo_x@SnO_2$ (Inset: equivalent circuit fitting)and re-oxidation.

The improved HER activity of $Mo_x@SnO_2$ can be attributed to two key factors. First, the presence of $[Mo_7O_{24}]^{6-}$ during synthesis presumably restricts the growth of the SnO_2 core, leading to smaller nanoparticles with a larger surface area, which can expose more catalytically active sites. Second, the synergistic electronic interaction between anionic and redox-active POM and the SnO_2 core enhances charge delocalization and electron-transfer ability. Further, the anionic POMs present on the surface of the material behave as proton adsorption centres and show improved proton adsorption ability. In addition, the redox-active properties of POMs enhance the electron delocalisation during HER, and accelerates the electrokinetic improving the electrocatalytic process. Overall, the electrochemical parameters, including lower overpotential, smaller Tafel slope, larger C_{dl}, and lower charge-transfer resistance, collectively demonstrate that $Mo_x@SnO_2$ is more active than pure SnO_2 and efficient electrocatalyst for HER under mild acidic pH conditions (Table S4).

3.4. Post-catalytic study

The structural and compositional stability of $Mo_x@SnO_2$ after long-term CA-HER study was confirmed by post-catalytic PXRD, FT-IR, and ICP-OES analysis of the used electrode and electrolyte solution (Figure 5a-5d). The PXRD pattern of the used $Mo_x@SnO_2$/CC electrode showed almost identical PXRD patterns like the as-synthesised sample. No additional reflections or no spectral broadening confirmed the retention of tetragonal SnO_2 core in the used electrode after 60 h CA-HER (Figure 5c). FT-IR analysis further revealed the retention of the characteristic broad [Sn–O] vibration band that appeared at 613 cm^{-1}, which is the signature of the [Sn–O] vibration of the SnO_2 core.[28] The bands at 946 and 899 cm^{-1} could be assigned to the $[M{=}O]_t$ and Mo–O–Mo bending [Mo–O] vibration bands[41] of the heptamolybdate cluster, indicating the presence of POM on the SnO_2 surface and the structure of the material is largely preserved after CA-HER (Figure 5d). After 60 h CA-HER, the optical spectrum of the electrolyte was further examined which showed an broad absorption band within 275-300 nm, which can be attributed to the molybdate, as correlated to standard molybdate or heptamolybdate samples (Figure S6).[42] Furthermore, to quantify the Mo and Sn possibly present in electrolyte after 60 h CA-HER electrolysis, the electrolyte was further analyzed through ICP-OES. ICP-OES analysis of the electrolyte suggests approximately 6.8% molybdenum leaching after 60 h of electrolysis (Figure 5a). In comparison, only 0.8% Sn leaching was detected, indicating that the SnO_2 core remains intact against dissolution. At the same time, a fraction of the surface-bound molybdate cluster undergoes gradual leaching during long-term electrolysis.

Just Accepted

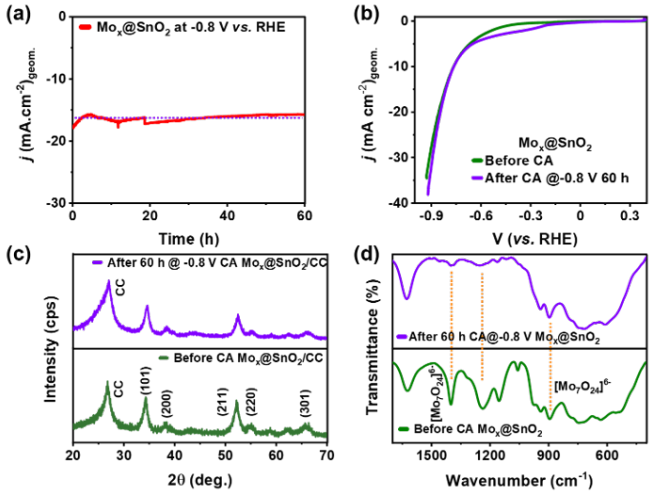


Figure 5. (a) Chronoamperometric HER study using Mo$_x$@SnO$_2$/CC for 60 h at a constant potential of -0.8 V (vs. RHE). (b) Comparison of LSV before and after CA of Mo$_x$@SnO$_2$/CC. (c) PXRD data and (d) FT-IR spectra of Mo$_x$@SnO$_2$/CC electrode before and after 60 h of CA-HER.

4 Conclusion

Heptamolybdate-stabilised SnO_2 nanocore material was reported earlier as an efficient cathode material for studying NO_3RR to NH_3. In this study, this unique material was presented as an excellent solution-state proton conductor, achieving 32.47×10^{-3} S cm^{-1} at pH 3.65 and 318 K. An extremely low activation energy barrier of 0.13 eV highlighted the facile proton relay across the Mo$_x$@SnO$_2$. A comparative study with bare SnO_2 and POM-stabilized SnO_2 has shown that the presence of Anderson-type heptamolybdate not only facilitates the proton flow but also enhances the adsorption of protons, which makes it an excellent proton reduction catalyst. The low overpotential, Tafel slope, charge-transfer resistance, and higher ECSA values are responsible for the better HER performance of Mo$_x$@SnO$_2$ than that of SnO_2. The presence of POM clusters covalently linked to SnO_2 not only stabilised the SnO_2 but also made the Mo$_x$@SnO$_2$ an active and efficient electrocatalyst for clean hydrogen production. Although the performance of this material can't supersede the benchmark noble-metal-based catalyst, Pt/C, it is an example of a non-precious metal POM-based catalyst, whose advantage lies in the relative improvement of proton conduction and HER compared to bare SnO_2.

Electronic Supplementary Material: Supplementary material (please provide a brief detail of the ESM) is available in the online version of this article at https://doi.org/10.26599/POM.2026.9140175.

Data availability

All data needed to support the conclusions in the paper are presented in the manuscript and/or the Electronic Supplementary Material. Additional data related to this paper may be requested from the corresponding author upon request.

Acknowledgements

L.M. thanks IIT Delhi for his fellowship. H. K. B. (ID: 1403207) sincerely acknowledges PMRF, Govt. of India, for their fellowship and research contingency. The authors thank the HRTEM and FESEM facilities of CRF, IIT Delhi.

Declaration of competing interests

The other contributing author(s) report no conflict of interest in this work.

Author contribution statement

LM: Data curation, project administration, validation, writing manuscript, and experimental design. HKB: Data curation, validation, experimental design, writing manuscript. BC: Project administration, validation, writing manuscript. All the authors have approved the final manuscript.

Use of an AI statement

During the preparation of this work, the authors used ChatGPT to revise the manuscript. After using this tool, the authors reviewed and edited the content as needed and take full responsibility for the content of the publication.

References

(1) Saha, A.; Sahoo, R.; Pal, S. C.; Uchida, S.; Das, M. C. Polyoxometalates (POMs) as Proton Conductors. *ACS Energy Lett.* **2025**, *10* (4), 1958–1998.

(2) Zhang, H.; Wang, Y.; Shi, Y.; Zhang, Y.; Yang, Y.; Wang, Y.; Cui, Y.; Guo, J.; Zhang, P.; Sun, L. Recent Advances in Polyoxometalate-Based Proton Conducting Materials: Design Strategies, Conduction Mechanisms, Structure-Function Relationships and Future Perspectives. *Nano Res.* **2025**, *18* (9), 94907743.

(3) Unnikrishnan, P. M.; Basu, O.; Nasani, R.; Das, S. K. Giant {Mo 132} Polyoxometalate Isolated with Diverse Organic Cations: A Systematic Proton Conductivity Study. *Dalt. Trans.* **2025**, *54* (5), 2166–2176.

(4) Wang, B.; Lin, R.-B.; Zhang, Z.; Xiang, S.; Chen, B. Hydrogen-Bonded Organic Frameworks as a Tunable Platform for Functional Materials. *J. Am. Chem. Soc.* **2020**, *142* (34), 14399–14416.

(5) Feng, X.; Ding, X.; Jiang, D. Covalent Organic Frameworks. *Chem. Soc. Rev.* **2012**, *41* (18), 6010–6022.

(6) Furukawa, H.; Cordova, K. E.; O'Keeffe, M.; Yaghi, O. M. The Chemistry and Applications of Metal-Organic Frameworks. *Science.* **2013**, *341* (6149), 1230444.

(7) Yoon, M.; Suh, K.; Natarajan, S.; Kim, K. Proton Conduction in Metal–Organic Frameworks and Related Modularly Built Porous Solids. *Angew. chemie Int. Ed.* **2013**, *52* (10), 2688–2700.

(8) Zhang, S.; Lu, Y.; Sun, X.-W.; Li, Z.; Dang, T.-Y.; Zhang, Z.; Tian, H.-R.; Liu, S.-X. Purely Inorganic Frameworks Based on Polyoxometalate Clusters with Abundant Phosphate Groups: Single-Crystal to Single-Crystal Structural Transformation and Remarkable Proton Conduction. *Chem. Commun.* **2020**, *56* (3), 391–394.

(9) Liu, J.; Han, Q.; Chen, L.; Zhao, J.; Streb, C.; Song, Y. Aggregation of Giant Cerium–Bismuth Tungstate Clusters into a 3D Porous Framework with High Proton Conductivity. *Angew. Chemie Int. Ed.* **2018**, *57* (28), 8416–8420.

(10) Priya, L.; Unnikrishnan, P. M.; Bommakanti, S.; Pallepogu, R.; Das, S. K. A Vapor–Liquid Interface Reaction Leading to the Isolation of an "Oxo-Rich"{Mo$_{36}$} Polyoxometalate Compound for Proton Conductivity Studies. *Inorg. Chem.* **2026**, *65* (27), 15340–15345.

(11) Iwano, T.; Miyazawa, S.; Osuga, R.; Kondo, J. N.; Honjo, K.; Kitao, T.; Uemura, T.; Uchida, S. Confinement of Poly (Allylamine) in Preyssler-Type Polyoxometalate and Potassium Ion Framework for Enhanced Proton Conductivity. *Commun. Chem.* **2019**, *2* (1), 9.

(12) Li, S.; Zhao, Y.; Knoll, S.; Liu, R.; Li, G.; Peng, Q.; Qiu, P.; He, D.; Streb, C.; Chen, X. High Proton-conductivity in Covalently Linked Polyoxometalate-organoboronic Acid-polymers. *Angew. Chemie*

Just Accepted

Int. Ed. **2021**, *60* (31), 16953–16957.

(13) Miras, H. N.; Vilà-Nadal, L.; Cronin, L. Polyoxometalate Based Open-Frameworks (POM-OFs). *Chem. Soc. Rev.* **2014**, *43* (16), 5679–5699.

(14) Nakamura, O.; Kodama, T.; Ogino, I.; Miyake, Y. High-Conductivity Solid Proton Conductors: Dodecamolybdophosphoric Acid and Dodecatungstophosphoric Acid Crystals. *Chem. Lett.* **1979**, No. 1, 17–18.

(15) Unnikrishnan, P. M.; Premanand, G.; Das, S. K. Polyoxometalate-Driven Assembly of Inorganic–Organic Hybrid Materials: Proton Conductivity Studies. *J. Chem. Sci.* **2025**, *137* (1), 13.

(16) Premanand, G.; Jana, D.; Unnikrishnan, P. M.; Das, S. K. Hexagonal Mo Bronze: Single Crystal Structures, Electrocatalytic Hydrogen Evolution, and Proton Conductivity. *Inorg. Chem.* **2024**, *63* (23), 10671–10681.

(17) Kolli, H. K.; Das, A.; Jana, D.; Saraswat, R.; Jana, T.; Das, S. K. Giant Polyoxometalate Acting as a Nanofiller into a Polymer to Fabricate Proton Exchange Membranes Exhibiting Super Proton Conductivity. *Inorg. Chem.* **2025**, *64* (14), 7148–7163.

(18) Chaudhary, M.; Kumar, S.; Mallick, L.; Chakraborty, B. Facile Proton Relay in the Triazole Framework to Promote the Electrocatalytic Hydrogen Evolution Reaction. *ACS Appl. Polym. Mater.* **2023**, *5* (10), 8235–8240.

(19) Mahata, A.; Mallick, L.; Mehta, I.; Kumari, N.; Bhattacharya, S.; Chakraborty, B. Intrinsic Proton Relay in Poly-Phosphamides to Bolster Proton Exchange Membrane Fabrication and Electrocatalytic Proton Reduction. *J. Mater. Chem. A* **2025**, *13* (27), 21480–21492.

(20) Morla, K. S.; Thakre, D.; Mourya, A. K.; Singh, P.; Karnamkkott, H. S.; Ahamed, S.; Sahoo, S.; Bhattacharya, I.; Banerjee, S.; Sarma, D. A Mixed Metallic and Mixed Valence Mo V4 V IV2 V III2 Complex as an Electron Transfer Photo-Catalyst for the Hydrogen Evolution Reaction. *Chem. Commun.* **2025**, *61* (49), 8919–8922.

(21) Bhunia, S.; Rana, A.; Hematian, S.; Karlin, K. D.; Dey, A. Proton Relay in Iron Porphyrins for Hydrogen Evolution Reaction. *Inorg. Chem.* **2021**, *60* (18), 13876–13887.

(22) Saira, Y.; Li, Z.; Zhu, Y.; Liu, Q.; Luo, W.; Wang, Y.; Gong, M.; Fu, G.; Tang, Y. Low-Loaded Ru on Hollow SnO 2 for Enhanced Electrocatalytic Hydrogen Evolution. *Chem. Commun.* **2024**, *60* (20), 2768–2771.

(23) Singh, C.; Haldar, A.; Basu, O.; Das, S. K. Devising a Polyoxometalate-Based Functional Material as an Efficient Electrocatalyst for the Hydrogen Evolution Reaction. *Inorg. Chem.* **2021**, *60* (14), 10302–10314.

(24) Jana, D.; Kolli, H. K.; Sabnam, S.; Das, S. K. Efficient Homogeneous Electrocatalytic Hydrogen Evolution Using a Ni-Containing Polyoxometalate Catalyst. *Chem. Commun.* **2021**, *57* (77), 9910–9913.

(25) Anjass, M.; Lin, C.-G.; White, M.; Newton, G. N.; Song, Y.-F.; Streb, C. Polyoxometalates for Redox Chemistry. *Nat. Rev. Methods Prim.* **2026**, *6* (1), 73.

(26) Wang, T.; Wang, W.; Xuan, M.; Ma, X.; Labidi, A.; Chen, G. Polyoxometalates and Their Derivatives: Structural Tuning of Versatile Electrocatalysts for Water Splitting. *Energy Mater.* **2026**, *6* (8), N-A.

(27) Ravi, A.; Mulkapuri, S.; Das, S. K. Hydroxylated Polyoxometalate with Cu (II)-and Cu (I)-Aqua Complexes: A Bifunctional Catalyst for Electrocatalytic Water Splitting at Neutral PH. *Inorg. Chem.* **2023**, *62* (32), 12650–12663.

(28) Mallick, L.; Annadata, H. V; Chakraborty, B. Vacancy-Rich SnO2 Quantum Dot Stabilized by Polyoxomolybdate as Electrocatalyst for Selective NH_3 Production. *ACS Appl. Mater. Interfaces* **2024**, *16* (25), 32385–32393.

(29) Basak, H. K.; Adak, M. K.; Rajput, A.; Chakraborty, B. Low Pt Loading on Wolframite-Type NiWO4 to Excel the Electrocatalytic Water Splitting and Ammonia Oxidation Reaction. *ACS Appl. Mater. Interfaces* **2025**, *17* (6), 9391–9406.

(30) McCrory, C.L. C.; Jung, S.; Peters, J. C.; Jaramillo, T. F. Benchmarking Heterogeneous Electrocatalysts for the Oxygen Evolution Reaction. **2013**, *135* (45), 16977–16987.

(31) Basak, H. K.; Kamboj, B.; Patra, J.; Ghosh, D.; Chakraborty, B. Enhancing the Valence Band Charge Localization via Zinc Doping into $MnWO_4$ to Promote Selective Ammonia Electrooxidation. *J. Mater. Chem. A* **2026**, 14, 9492–9509.

(32) Mallick, L.; Chakraborty, B. Ionic Γ-FeO (OH) Nanocrystal Stabilized by Small Isopolymolybdate Clusters as Reactive Core for Water Oxidation. *Chem. Eur. J.* **2023**, *29* (6), e202203033.

(33) Samanta, K.; Mallick, L.; Chakraborty, B. Stabilization of Nickel-Doped Iron-Oxy-Hydroxide Core in Water by Heptamolybdate Ions to Improve the Electrochemical Oxygen Evolution Reaction. *ACS Appl. Energy Mater.* **2024**, *7* (1), 335–345.

(34) Wan, N.; Lu, X.; Wang, Y.; Zhang, W.; Bai, Y.; Hu, Y.-S.; Dai, S. Improved Li Storage Performance in SnO_2 Nanocrystals by a Synergetic Doping. *Sci. Rep.* **2016**, *6* (1), 18978.

(35) Cheng, D.; Li, K.; Zang, H.; Chen, J. Recent Advances on Polyoxometalate-based Ion-conducting Electrolytes for Energy-related Devices. *Energy Environ. Mater.* **2023**, *6* (2), e12341.

(36) Li, C.; Yamaguchi, K.; Suzuki, K. Ligand-Directed Approach in Polyoxometalate Synthesis: Formation of a New Divacant Lacunary Polyoxomolybdate γ-$[PMo_{10}O_{36}]^{7-}$. *Angew. Chemie* **2021**, *133* (13), 7036–7040.

(37) Slade, R. C. T.; Pressman, H. A.; Skou, E. Ac and Dc Conductivity Studies of Pelletised 12-Tungstophosphoric Acid and 12-Tungstosilicic Acid Hexahydrates. *Solid State Ionics* **1990**, *38* (3–4), 207–211.

(38) Qian, X.; Tong, X.; Wu, Q.; He, Z.; Cao, F.; Yan, W. Synthesis and Electrochemical Properties of Substituted Heteropoly Acid with Dawson Structure $H_7[In(H_2O)P_2W_{17}O_{61}]\cdot 23H_2O$. *Dalt. Trans.* **2012**, *41* (33), 9897–9900.

(39) Janik, M. J.; Campbell, K. A.; Bardin, B. B.; Davis, R. J.; Neurock, M. A Computational and Experimental Study of Anhydrous Phosphotungstic Acid and Its Interaction with Water Molecules. *Appl. Catal. A Gen.* **2003**, *256* (1–2), 51–68.

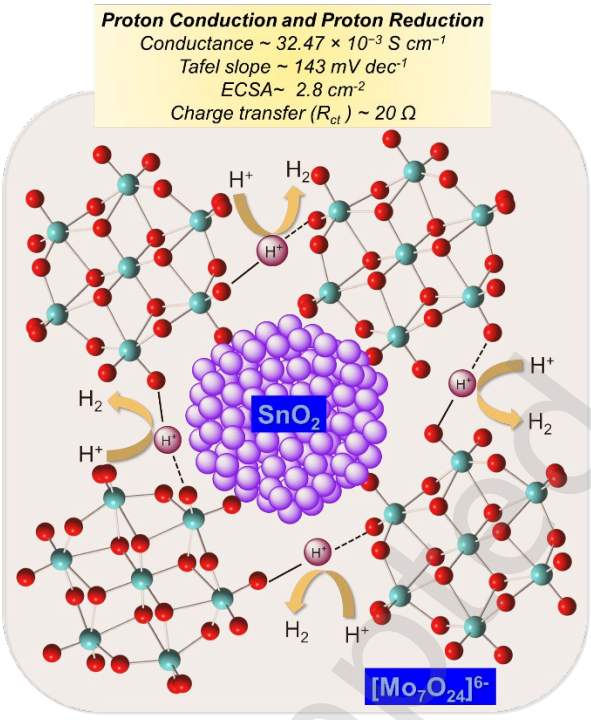
(40) Cui, Y.-M.; Zhu, Y.-J.; Sun, J.; Wu, D.; Wang, X.; Wu, X.-S.; Su, Z.-M. Swift Proton Release Enhancing Proton Conductivity in Anderson-Polyoxometalates-Based Metal–Organic Frameworks. *ACS Mater. Lett.* **2024**, *6* (9), 4255–4261.

(41) Mallick, L.; Kumari, A.; Ghosh, D.; Chakraborty, B. Visible-Light-Driven Ammonia Photosynthesis on Mo_7-Cluster Stabilized CeO2 Nanocore Through Interfacial Charge Transfer. *Small* **2026**, *22* (2), e13123.

(42) Rajput, A.; Kumari, A.; Basak, H. K.; Ghosh, D.; Chakraborty, B. Tracking the Active Phase and Reaction Pathway of the OER Mediated by an MnMoO4 Microrod Electro (Pre)-Catalyst. *J. Mater. Chem. A* **2024**, *12* (44), 30810–30820.

Just Accepted

Anderson-type ammonium heptamolybdate-protected SnO_2 quantum dots enable proton adsorption, relay and reduction to produce clean hydrogen.



Just Accepted